Korean J. Chem. Eng., 38(2), 326-336 (2021)
DOI: 10.1007/s11814-020-0708-x

pISSN: 0256-1115
eISSN: 1975-7220

Synthesis of mesoporous 2-line ferrihydrite/γ-Al_2O_3 hybrid adsorbent for the effective adsorption of phosphate for water remediation

Seung-Joon Yoo†

Resources Development Research Institute, Department of Earth Resources and Environmental Engineering, Hanyang University, 222 Wangsimni-ro, Seongdong-gu, Seoul 04763, Korea
(*Received 22 September 2020 • Revised 3 November 2020 • Accepted 5 November 2020*)

Abstract−A 2-line ferrihydrite/γ-Al_2O_3 hybrid adsorbent (Fh/γ-Al_2O_3 hybrid adsorbent) precipitated on 10 wt% of γ-Al_2O_3 seed for the effective adsorption of phosphate in water was synthesized from wastewater containing ferric sulfate. The use of γ-Al_2O_3 seeds for particle initiation made it possible to prepare larger particles that would allow a liquid to flow through. The synthesized Fh/γ-Al_2O_3 hybrid adsorbent was characterized by X-ray diffraction, ^{27}Al-MAS NMR, N_2 adsorption/desorption, SEM analysis, and EpHL measurements. The adsorption performance of phosphate on the synthesized Fh/γ-Al_2O_3 hybrid adsorbent was evaluated by batch and column tests at phosphate concentration below 10 ppm, which corresponds to the actual phosphate concentration of natural systems. The adsorption mechanism suggested by the batch test was in good agreement with the Langmuir adsorption model, with a maximum adsorption capacity of 33.2 mg/g. On the other hand, the experiment with the column obtained a maximum adsorption capacity of 33.6 mg/g for a volumetric flow rate of 10.25 BV/min and an influent phosphate concentration of 4.75 ppm on 0.5 g of adsorbent. The Fh/γ-Al_2O_3 hybrid adsorbent was shown to have superior adsorption characteristics to those of other previous research in terms of cost, adsorption efficiency, contact time, maximum adsorption capacity, and desorption efficiency of 95% from the experimental condition based on the surface characterization of the adsorbent.

Keywords: 2-Line Ferrihydrite/γ-Al_2O_3 Hybrid Adsorbent, Adsorption, Desorption, EpHL, Phosphate, Batch, Column

INTRODUCTION

Ferrihydrite (Fh) is generally a poorly crystalline Fe(III) hydroxide whose particles have nanometric dimensions. Due to its poor crystallinity, X-ray diffraction patterns consist of low intensity and broad reflections. On the basis of the number of peaks observed in XRD patterns, two different ferrihydrites are defined as 6-line and 2-line. The 6-line ferrihydrite is more ordered and XRD pattern consists of 6 well-defined peaks, but 2-line ferrihydrite is very poorly crystallized and the XRD pattern consists of two broad peaks [1]. Typically, the crystallite size is between 1.5 and 10 nm [2].

These structures are determined by the size difference of the constitutive particles. A previous study showed that poorly crystallized 2-line Fh material consisted of smaller particles with a correspondingly larger surface area than 6-line Fh material, which is more ordered and relatively well-defined six peaks. In its ideal form, this structure contains 20% tetrahedrally and 80% octahedrally coordinated iron [3].

Based on this result, the 2-line Fh structure has found widespread use and has a high affinity and capacity for the adsorption of a variety of ions such as chloride, nitrate, and phosphate dissolved in water [4-6], metals such as copper and zinc from buildings and downpipes [7], arsenic in ground and drinking water [8], heavy metals (Cr, U, Cd, Pb) [9-12] and toxic elements (Sb, V, Mo, Se) [13-16] in industrial wastewater, offensive odors (H_2S, ozone, THMs, siloxanes) [17-20], and fluorine [21].

The high adsorption ability of the 2-line Fh structure has resulted in its becoming known as a healing agent for environmental remediation.

In terms of the removal of dissolved nutrients to prevent eutrophication in water, various methods, such as filtration, chemical precipitation, ion exchange, and biological treatment, have been suggested but the most promising method is adsorption technology because of its simplicity, low cost, high efficiency, and facile operation and maintenance.

In adsorption technology, various adsorbents such as tourmalines [22], clay [23], magnetite [24], zeolite [25], fly ash [26], and iron oxide [27], have been used to remove phosphate. These adsorbents have their advantages and disadvantages under the similar phosphate solution, as shown in Table 1.

The most pivotal aspect of adsorption technology is to design the adsorbent such that it is appropriate for the purpose and objective of adsorption. We aimed to optimize the design of the 2-line Fh/γ-Al_2O_3 hybrid adsorbent by controlling various physical properties such as its particle size, affinity, PZC (point of zero charge), specific surface area, total pore volume, and pore size distribution to ultimately obtain an effective adsorbent for water treatment.

In the case of liquid-phase adsorption, physical properties such as the apparent particle size, pore size, and specific surface area are critically important because they are directly related to the adsorption capacity, the adsorption velocity, and the adsorption efficiency. Among these physical properties, a suitable particle size is pivotal for water treatment because a column containing small particles would prevent the water from passing through, whereas larger parti-

†To whom correspondence should be addressed.
E-mail: sjyoo001@hanyang.ac.kr

Table 1. Efficiency of phosphate removal by various adsorbents

Raw material	Adsorbent	Surface area (m^2/g)	Adsorbent dosage (g/L)	Max. adsorption capacity (mg/g)	Initial phosphate conc. (mg/L)	pH	Adsorption efficiency (%)	Ref.
Tourmaline, $LaCl_3$	La-modified tourmaline	15.59	1	108.7	5	7	90	22
Clay, Corn starch, CaO	Tablet porous material (TPM)	15.4	4	4.39	5-50	5-9	89.08	23
$LaCl_3$, TEOS, $FeCl_3$,$Fe_2(SO_4)_3$	$La_2O_3/SiO_2/Fe_3O_4$	47.73	>0.2	27.8	2	5-9	>95	24
Natural zeolite, $Ca(OH)_2$-	$Ca(OH)_2$-Zeolite	-	10	6.06-8.79	10	7	97.6	25
Fly ash, palygorskite	Acid-modified fly ash-palygorskite	-	2	13.3 10.5	10	7.5	-	26
$FeCl_3$ $ZrOCl_2$	Fe-Zr oxide	339	0.2	33.4	10	5.5	93	27

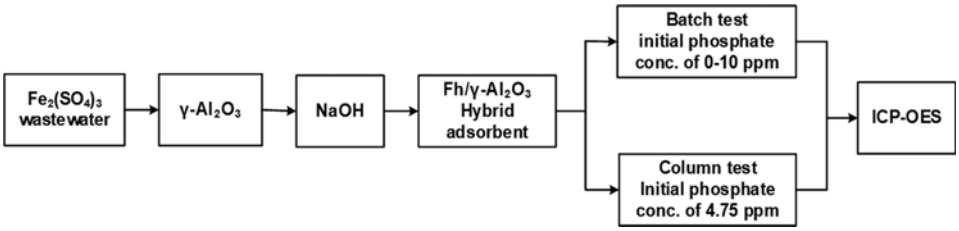

Fig. 1. Flow diagram on the overall adsorption process from synthesis of Fh/γ-Al_2O_3 hybrid adsorbent to the performance test.

cles would allow the water to efficiently pass through the macropores between adsorbent particles.

Accordingly, we implemented a new idea of initially adding γ-Al_2O_3 powder as a seed to induce the formation of larger particles during the preparation of the Fh/γ-Al_2O_3 hybrid adsorbent with mesopores for water treatment. The γ-Al_2O_3 powder, well known as an effective adsorbent for the phosphate absorption, was used as a seed [28].

Fig. 1 shows the flow diagram of the overall adsorption process from the synthesis of Fh/γ-Al_2O_3 hybrid adsorbent to the performance test.

Many adsorbents have been studied to determine their effectiveness for removing phosphate. In particular, GEH-104, commercialized by GEH Wasserchemie GmbH, is a representative adsorbent. It has a maximum adsorption capacity of 14.1 mg/g, as determined by its Langmuir adsorption isotherms [29]. Other research found the maximum adsorption of GEH-104 to be 21.88 mg/g for a phosphate concentration range of 1 to 5 mg/L [30].

The performance of the adsorbent is determined by the adsorption affinity between the adsorbent and adsorbate as well as the maximum adsorption capacity. The adsorption affinity is additionally determined by certain factors such as the PZC of the adsorbent and the pH of the solution.

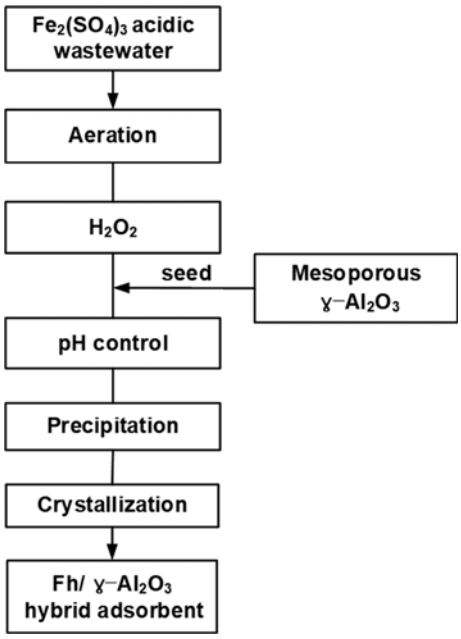

Fig. 2. Process flow diagram for the synthesis of Fh/γ-Al_2O_3 hybrid adsorbent.

EXPERIMENTAL

1. Materials

Fig. 2 presents the process of synthesizing the 2-line Fh/γ-Al_2O_3 hybrid adsorbent in the form of a flow diagram.

The Fh/γ-Al_2O_3 hybrid adsorbent was synthesized from acidic ferric sulfate wastewater by using the following procedure. The ferric sulfate solution was oxidized by aeration and the addition of

hydrogen peroxide (H_2O_2, 30%, Merck) at 70 °C and 500 rpm. Then, γ-Al_2O_3 powder (anhydrous γ-Al_2O_3, Merck) was added (10 wt%) to the oxidized ferric sulfate solution as a seed for particle formation.

In the next step, the pH of the ferric sulfate solution was controlled at pH 6.0 by adding an aqueous solution of sodium hydroxide (NaOH, 99%, Merck). As a result, Fh particles rapidly precipitated on the surface of the γ-Al_2O_3 seed particles and these particles continued to grow during the crystallization step. The Fh/γ-Al_2O_3 hybrid adsorbent obtained in this way was washed by deionized water three or four times and dried at 130 °C for 24 h.

2. Adsorption Performance Test

Batch and column adsorption experiments were carried out to measure the adsorption performance on the synthesized Fh/γ-Al_2O_3 hybrid adsorbent.

The batch experiment was conducted at 298 K using phosphate solutions of which the concentration ranged from 0.1 to 10 mg/L by adding *ortho*-phosphoric acid (H_3PO_4, 85.00%, Merck) to deionized water. The adsorbent (2.5 mg) was added to 10 mL of phosphate solution in all the batch experiments and then adequately agitated for 5 h using a roller mixer. After agitation, the phosphate concentration of the sample was analyzed by ICP-OES after solid-liquid separation.

The column experiment was conducted by using an adsorption apparatus with a U-type column to enable the solution to pass through the adsorbent layer continually at a constant flow rate by applying potential energy as shown in Fig. 3.

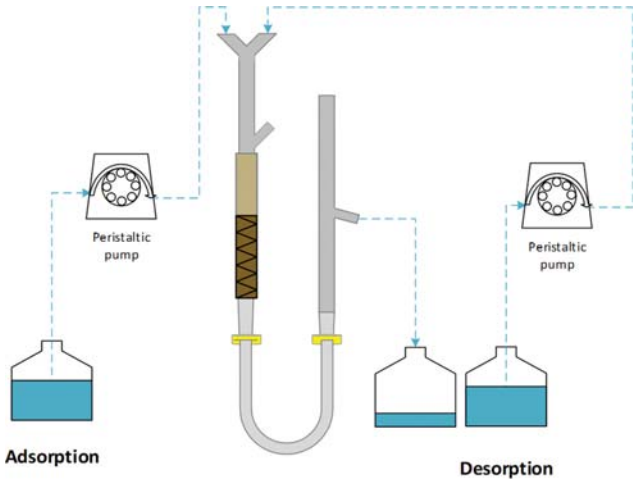

Fig. 3. Schematic diagram of column adsorption/desorption apparatus.

The particle size of the adsorbent used in the column test was classified to be in the range of 180-500 μm. A 12-mm column was packed with 0.5 g of adsorbent. A phosphate solution with an initial concentration of 4.75 mg/L, prepared from *ortho*-phosphoric acid (H_3PO_4, 85.00%, Merck), was injected into the upper column zone by a peristaltic pump at 298 K. The volumetric flow rate was constantly maintained at 10.25 BV/min (3.09 mL/min).

3. Analysis

The X-ray diffraction patterns were recorded using an X-ray diffractometer (X'PERT-PRO MPD, Malvern PANalytical) equipped with a CuKα radiation source (λ=1.5406 Å) and generator settings of 30 mA and 40 kV.

The adsorbent structure was analyzed by ^{27}Al MAS NMR (400 MHz Avance II+ Bruker Solid-state NMR). The chemical shift was measured using a spinning rate of 13 kHz, a delay time of 1 s, a pulse length of 0.8 μs, a radio frequency of 104.26 MHz, and $AlCl_3$ (aq) for calibration (0 ppm).

Nitrogen adsorption and desorption analysis was conducted at 77 K using a Micromeritics (ASAP 2020) surface area and porosity analyzer after the sample was automatically degassed in the degassing port of the adsorption apparatus.

The PZCs (point of zero charges) of the γ-Al_2O_3, Fh adsorbent, and Fh/γ-Al_2O_3 hybrid adsorbent were measured by using the pH electrode of an Advanced Electrochemistry Meter (Orion VERSASTAR, Thermo Scientific). The adsorbent (1,000 m^2/L) was added to the water by adjusting the initial pH from 1 to 13. After shaking for 4 h, the final pH was measured by a pH meter.

The surfaces of the particles were visualized by employing field-emission scanning electron microscopy (HITACHI, SU8220).

The phosphate concentration was analyzed by inductively coupled plasma-optical emission spectrometry (ICP-OES, iCAP6000 Series, Thermo Scientific, UK). The standard solution was a commercial phosphate ion standard solution of 1,000 ppm supplied by KANTO.

RESULTS AND DISCUSSION

1. Adsorbent Characterization

The apparent particle size and pore diameter are highly import-

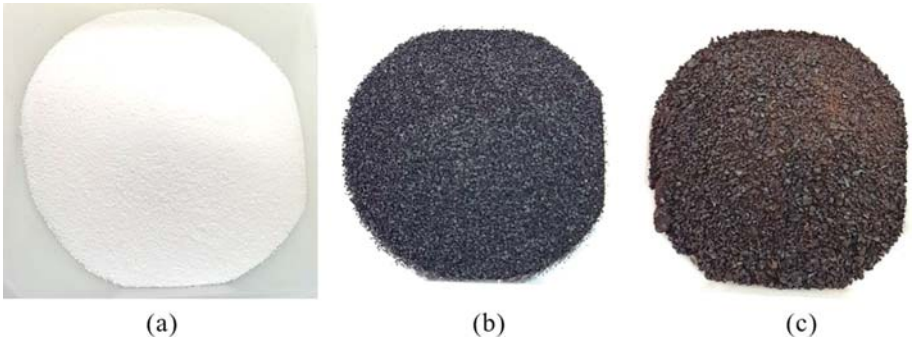

Fig. 4. Photographic images of the samples: (a) γ-Al_2O_3 (b) Fh adsorbent (c) Fh/γ-Al_2O_3 hybrid adsorbent.

ant in liquid-phase adsorption because they determine the flow rate and adsorption ability of the liquid. Generally, the particle size must exceed 100 μm to ensure smooth liquid flow and the pore diameter must be of the mesopore scale for effective adsorption.

Fig. 4(a)-(c) present photographic images of the γ-Al_2O_3, Fh adsorbent, and Fh/γ-Al_2O_3 hybrid adsorbent used in this experiment. Both the γ-Al_2O_3 and Fh adsorbent had a particle size of less than 100 μm. Accordingly, their particle sizes were too small to allow water to pass through the adsorbent layer. This problem necessarily had to be solved to enable an effective liquid-phase adsorbent to be developed.

To induce the formation of larger particles of the Fh/γ-Al_2O_3 hybrid adsorbent for liquid adsorption, we used γ-Al_2O_3 particles as a seed, as mentioned above in the experimental section. The addition of γ-Al_2O_3 particles accelerated the growth of Fh particles, which grew larger than without the addition, as shown in Fig. 4(c).

In the synthesized Fh/γ-Al_2O_3 hybrid particles, the γ-Al_2O_3 particles formed a core on which the Fh could accumulate, much in the way a large snowball would form. However, the existence of a core in the synthesized Fh/γ-Al_2O_3 hybrid particles was not apparent. Eventually, it became clear that the Fh/γ-Al_2O_3 hybrid particles had a core-shell structure as shown in the conceptual diagram of one of these particles in Fig. 5.

Fig. 6 presents the XRD patterns of γ-Al_2O_3, the Fh adsorbent, and the Fh/γ-Al_2O_3 hybrid material. The γ-Al_2O_3 powder that was used as a seed has a pseudo-crystalline phase with 2θ values of 32, 38, 46, 61, and 67°, and the Fh adsorbent has a poorly crystalline structure with two broad bands at 36 and 63° on its XRD pattern. The Fh/γ-Al_2O_3 hybrid material showed remarkable change in that the band at 38° on the XRD pattern of γ-Al_2O_3 completely disappeared, indicating that the 311 plane of the Al lattice of γ-Al_2O_3 was replaced by the Fe lattice of the Fh material.

Fig. 7 shows the result of the ^{27}Al MAS NMR analysis of γ-Al_2O_3 powder and the Fh/γ-Al_2O_3 hybrid adsorbent. The magnetic Fe nuclide of the Fh adsorbent is impossible to analyze using solid-state NMR because of the strong magnetic field of the NMR equipment. Accordingly, the Al nuclide in the core component of the Fh/γ-Al_2O_3 hybrid adsorbent was analyzed by ^{27}Al MAS NMR instead of the Fe component. In ^{27}Al MAS NMR analysis, the peak associated with the six-coordinated bonding of AlO_6 with an octahedral structure appears in the chemical shift range of 0 to 10 ppm, whereas the peak associated with the four-coordinated bond-

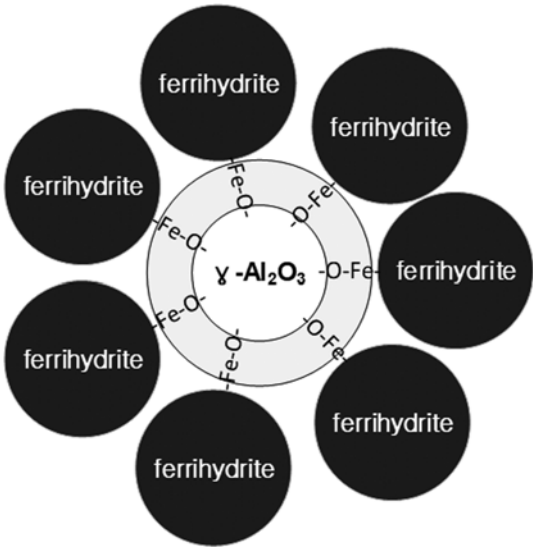

Fig. 5. Conceptual diagram of Fh/γ-Al_2O_3 hybrid particle.

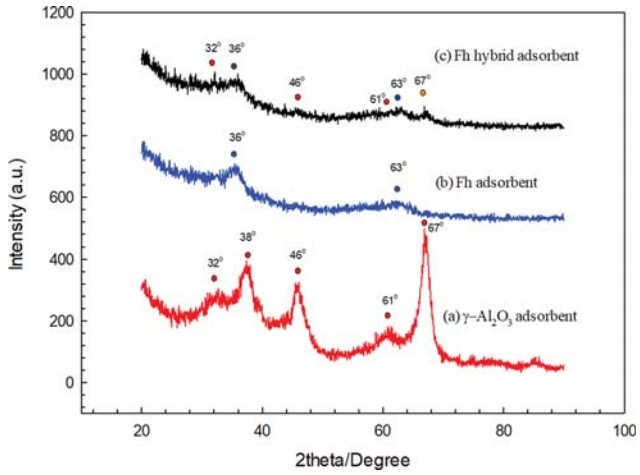

Fig. 6. XRD patterns of the samples: (a) γ-Al_2O_3 adsorbent (b) Fh adsorbent (c) Fh/γ-Al_2O_3 hybrid adsorbent.

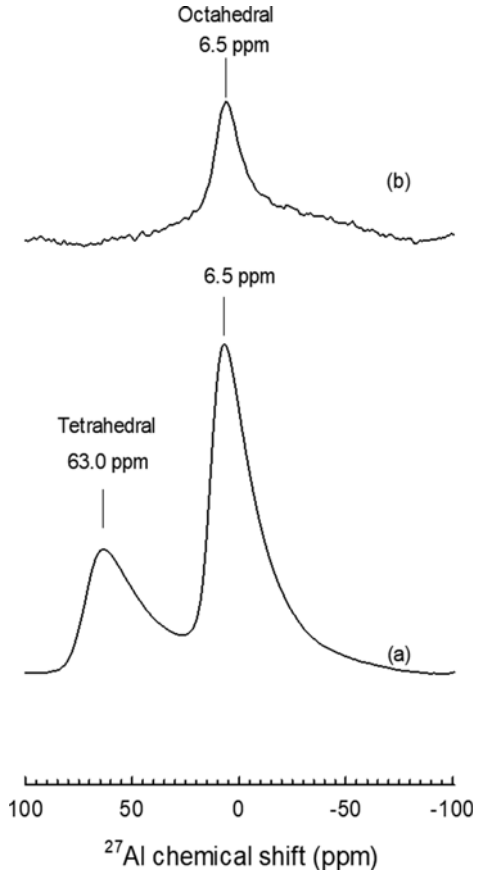

Fig. 7. ^{27}Al MAS NMR Spectra: (a) γ-Al_2O_3 (b) Fh/γ-Al_2O_3 hybrid adsorbent.

Table 2. Physical properties of the γ-Al_2O_3, Fh adsorbent, and Fh/γ-Al_2O_3 hybrid adsorbent

Property	Unit	γ-Al_2O_3	Fh adsorbent	Fh/γ-Al_2O_3 hybrid adsorbent
BET surface area	m^2/g	131	276	219
Langmuir surface area	m^2/g	168	356	283
Total pore volume	cm^3/g	0.24	0.20	0.22
Average pore size	nm	7.28	2.84	4.03

ing of AlO_4 with a tetrahedral structure appears in the range of 40 to 80 ppm as was previously demonstrated [31-36].

Our analysis revealed that the γ-Al_2O_3 structure contained both six-coordinated and four-coordinated bonding because peaks were detected at chemical shifts of 6.5 ppm and 63.0 ppm, as shown in Fig. 7(a). However, formation of the Fh/γ-Al_2O_3 hybrid adsorbent was accompanied by a structural change of γ-Al_2O_3. The tetrahedral AlO_4 structure disappeared after the synthesis of the Fh/γ-Al_2O_3 hybrid adsorbent. This indicates that the Fe nuclide of the Fh adsorbent replaced the Al nuclide bound to the tetrahedral structure of γ-Al_2O_3 particles.

Ultimately, the γ-Al_2O_3 not only acts as a seed to accelerate nucleation and growth, but also acts as a bridge to form a chemical bond between the γ-Al_2O_3 and Fh particles. Accordingly, we confirmed that the Fh/γ-Al_2O_3 hybrid adsorbent was not merely in a physically mixed state but that it involved chemically stable bonding.

The use of γ-Al_2O_3 as a seed to form a large snowball of the Fh/γ-Al_2O_3 hybrid adsorbent has many advantages: it increases the nucleation velocity and growth rate of precipitation, it allows microstructural characterization, and has a larger particle size with mesopores appropriate for water treatment.

The N_2 adsorption and desorption analysis in Table 2 shows that the γ-Al_2O_3 exhibited a microstructure with a Langmuir surface area of 168 m^2/g, BET surface area of 131 m^2/g, total pore volume of 0.24 cm^3/g, and average pore diameter of 7.28 nm. The microstructural characterization showed that the Fh adsorbent had a Langmuir surface area of 356 m^2/g, BET surface area of 276 m^2/g, total pore volume of 0.20 cm^3/g, and average pore diameter of 2.84 nm.

The microstructural characterization of the synthesized Fh/γ-Al_2O_3 hybrid adsorbent shows that it had a Langmuir surface area of 283 m^2/g, BET surface area of 219 m^2/g, total pore volume of 0.22 cm^3/g, and average pore diameter of 4.03 nm.

As mentioned, the Langmuir surface area of the Fh adsorbent was 356 m^2/g, whereas that of the Fh/γ-Al_2O_3 hybrid adsorbent was 283 m^2/g. The average pore diameter of the Fh/γ-Al_2O_3 hybrid adsorbent appeared to be larger at 4.03 nm than that of the Fh adsorbent at 2.84 nm. Thus, the average pore diameter of the Fh/γ-Al_2O_3 hybrid adsorbent was 1.19 nm larger than that of the Fh adsorbent.

The Fh adsorbent had an apparent particle size of less than 100 μm, which is unsuitable as it would not allow the water to pass through the adsorption layer.

Fig. 8 and Fig. 9 show the N_2 adsorption/desorption isotherms and pore size distribution for samples of the γ-Al_2O_3, Fh adsorbent, and Fh/γ-Al_2O_3 hybrid adsorbent. The N_2 adsorption-desorption isotherms are plotted in Fig. 8. The pore size distributions, deter-

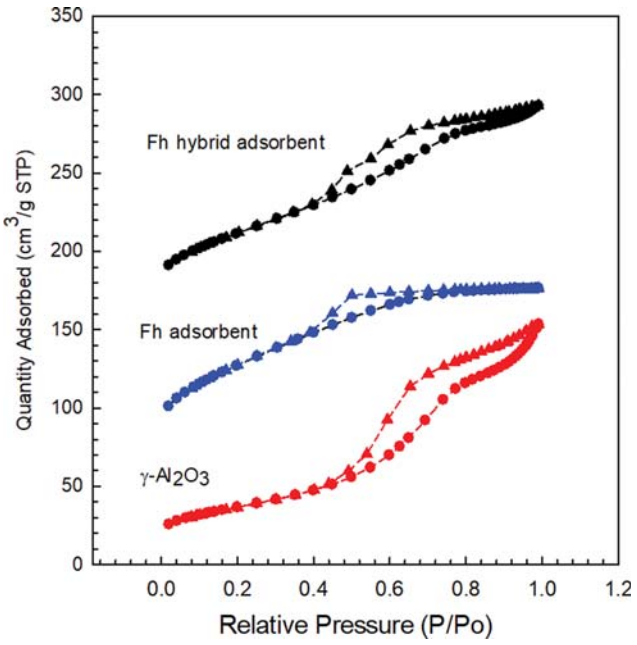

Fig. 8. Isotherm plots of γ-Al_2O_3, Fh adsorbent, and Fh/γ-Al_2O_3 hybrid adsorbent.

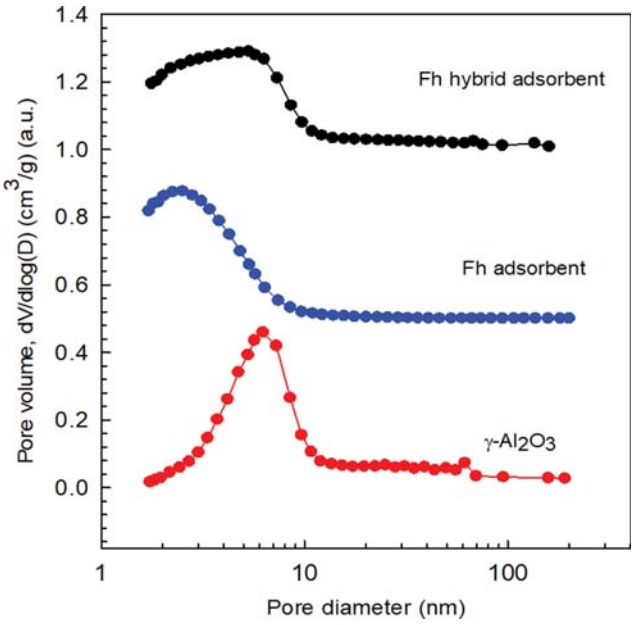

Fig. 9. Pore size distribution of γ-Al_2O_3, Fh adsorbent, and Fh/γ-Al_2O_3 hybrid adsorbent.

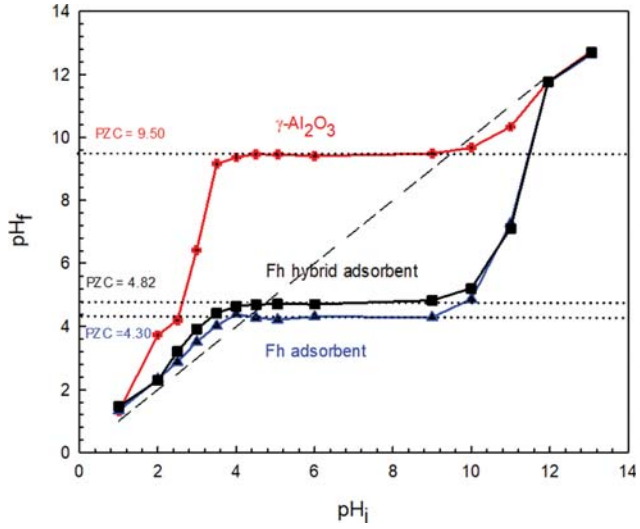

Fig. 10. PZCs of γ-Al_2O_3, Fh adsorbent, and Fh/γ-Al_2O_3 hybrid adsorbent by EpHL measurement [38,39].

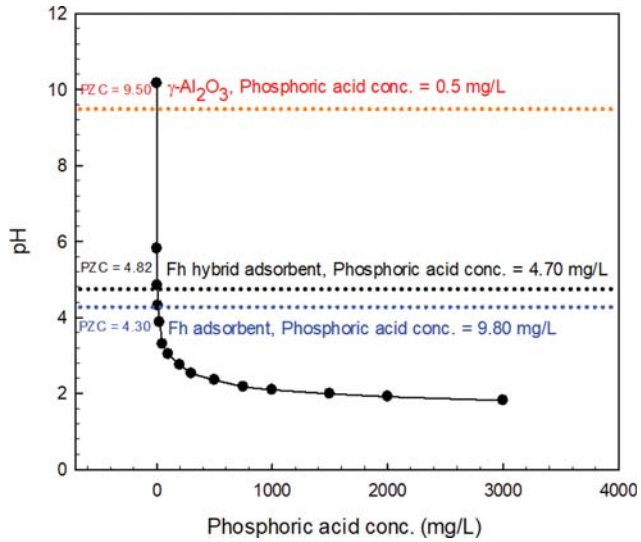

Fig. 11. Variation in the pH as a function of the phosphoric acid concentration.

mined by the BJH method, are plotted in Fig. 9.

The γ-Al_2O_3 seed served to enlarge the Fh particles when forming the Fh/γ-Al_2O_3 hybrid adsorbent and the resultant particles were more mesoporous. As a result, the Fh/γ-Al_2O_3 hybrid adsorbent had a particle diameter much larger than the Fh adsorbent.

As shown in Fig. 9, the Fh/γ-Al_2O_3 hybrid adsorbent mostly contains mesopores (4.03 nm) that are larger than the pores of the Fh adsorbent (2.84 nm). An average pore diameter of approximately 4.03 nm would be highly useful for the adsorption of phosphate, which has an ionic diameter of 1.196 nm [29,37]. In summary, we could verify that the design of the synthesized Fh/γ-Al_2O_3 hybrid adsorbent is appropriate for the effective adsorption of phosphate ions in water.

Fig. 10 shows the EpHL (equilibrium pH at high oxide loading) and PZC (point of zero charge) results obtained in previous research [38,39] on samples of the adsorbent. The final pH value differs from the initial value because of the uptake or release of a proton by the surface hydroxyl groups of the adsorbent. This phenomenon is visualized as a shift in pH in Fig. 10. The PZCs of the γ-Al_2O_3, Fh adsorbent, and Fh/γ-Al_2O_3 hybrid adsorbent, appeared to be 9.50, 4.30, and 4.82, respectively, as shown in Fig. 10. These results show that the γ-Al_2O_3 adsorbent had a positive surface charge at pH<4.45 and a negative surface charge at pH>8.97, and the Fh adsorbent had a positive surface charge at pH<3.98 and a negative surface charge at pH>8.97. The Fh/γ-Al_2O_3 hybrid adsorbent had positive and negative surface charges at pH<4.84 and pH> 8.53, respectively.

In liquid phase adsorption, the adsorption characteristics of the adsorbent depend on the pH of the solution, which varies according to the concentration of phosphoric acid as shown in Fig. 11. Our experiments showed that the phosphate concentration corresponding to the PZC of the Fh/γ-Al_2O_3 hybrid adsorbent was 4.82 mg/L. This result means that the initial phosphate concentration of 4.75 mg/L that was chosen for the column test is suitable to support electrostatic adsorption on the Fh/γ-Al_2O_3 hybrid adsorbent. On the other hand, the performance of the Fh adsorbent with a PZC value of 4.30 was assessed by using a phosphoric acid concentration of 9.80 mg/L. Therefore, the Fh adsorbent does not show strong electrostatic adsorption at the initial H_3PO_4 concentration of 4.75 mg/L.

Accordingly, the adsorption mechanism must consider the relation between the PZC value of the adsorbent and the pH value of the adsorbate as shown previously [40]. This value means that a phosphate concentration higher than 4.70 mg/L would favor strong electrostatic adsorption on the Fh/γ-Al_2O_3 hybrid adsorbent.

Conversely, at a phosphoric acid concentration lower than 4.70 mg/L, the strong electrostatic adsorption disappears and the adsorption ability is highly reduced.

Accordingly, the higher adsorption characteristics of the Fh/γ-Al_2O_3 hybrid adsorbent are the result of the addition of γ-Al_2O_3 with a PZC value of 9.50. This increased the PZC value of the Fh/γ-Al_2O_3 hybrid adsorbent from 4.30 to 4.82.

Finally, we confirmed the previous results by showing that the limit of the strong electrostatic adsorption was determined by the PZC value of the adsorbent [38,39].

The SEM photographic images in Fig. 12(a)-(c) show that the crystal structure γ-Al_2O_3 particles had a plate structure, particle size led spherical shape with the 50 to 100 μm as shown in Fig. 12(a). Meanwhile, the Fh particles in Fig. 12(b) were irregular, and nonuniform in size causing the amorphous structure. In the Fh/γ-Al_2O_3 hybrid adsorbent, the particles were almost uniform and increased to the larger particles than the Fh particles by the Fh precipitation on the γ-Al_2O_3 seeds as shown in Fig. 12(c).

2. Adsorption Studies

Phosphate is known to be a crucial eutrophication-causing material as a component of the nutrients dissolved in water. The adsorption performance was assessed by using a batch test and the fixed-bed column adsorption apparatus shown in Fig. 3. A comparison of the results of the batch and column adsorption experiments allowed us to clarify the adsorption roles of the adsorbent

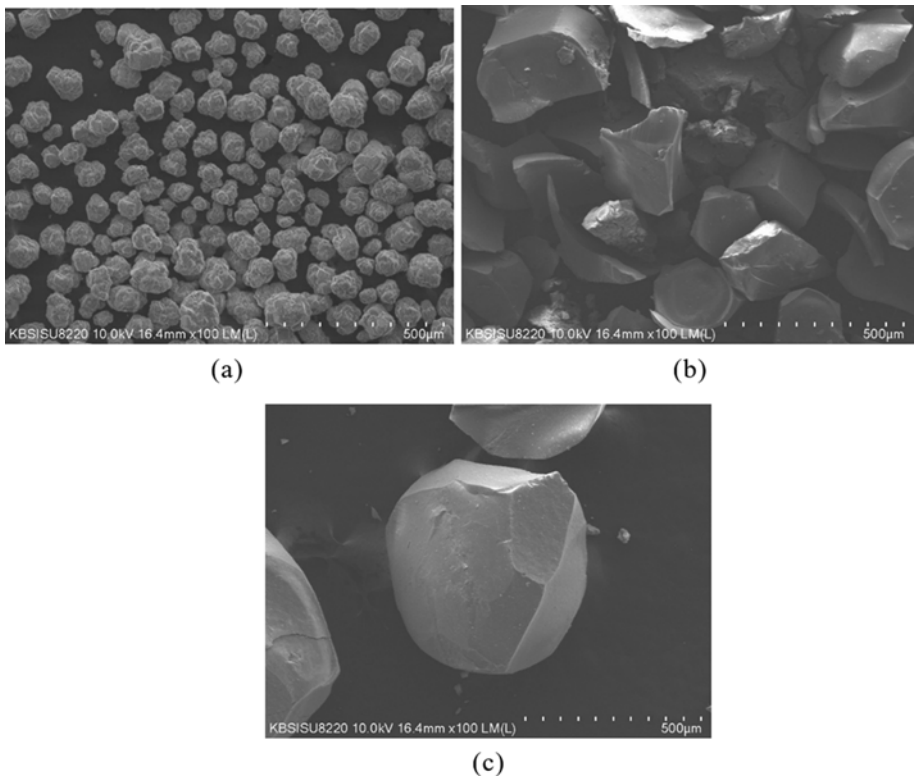

Fig. 12. SEM photographic images of the adsorption materials: (a) γ-Al_2O_3, (b) Fh adsorbent, and (c) Fh/γ-Al_2O_3 hybrid adsorbent.

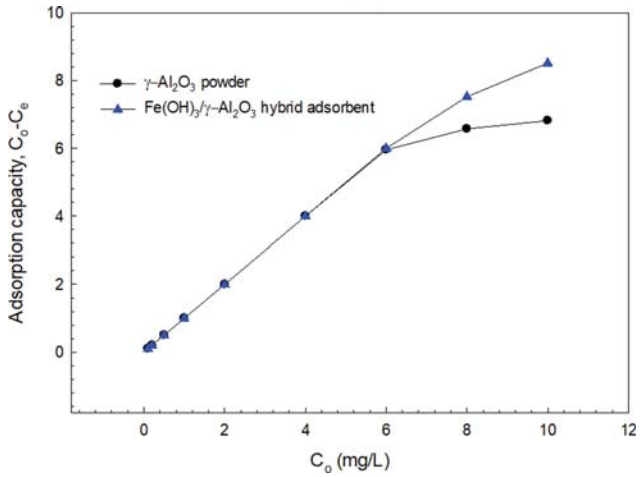

Fig. 13. Adsorption capacity of γ-Al_2O_3 and the Fh/γ-Al_2O_3 hybrid adsorbent as determined by the batch test.

and adsorbate. The batch experiment was conducted using initial phosphate concentrations ranging from 0 to 10 mg/L, which correspond to the level at which the eutrophication of rivers and lakes would be induced. Fig. 13 shows the adsorption capacity of γ-Al_2O_3 and the Fh/γ-Al_2O_3 hybrid adsorbent. The results show that the adsorption efficiency for both of these adsorbents is 100% until the phosphate concentration reaches 6 mg/L. At higher concentration, the adsorption characteristics of the Fh/γ-Al_2O_3 hybrid adsorbent are superior to those of γ-Al_2O_3. These experiments enabled us to confirm that the Fh/γ-Al_2O_3 hybrid adsorbent has adsorption characteristics that are excellent compared to those of γ-Al_2O_3.

The equilibrium adsorption capacity of phosphate, q_e (mg/g), was calculated by Eq. (1):

$$q_e = \frac{(C_o - C_e)V}{m} \ (mg/g) \tag{1}$$

where C_o and C_e are the initial and equilibrium phosphate concentrations (mg/L), V is the volume of the phosphate solution (mL), and m is the mass of the adsorbent (g).

The Langmuir [41] and Freundlich isotherm models [42] were applied to the experimental data to investigate the maximum amount that could theoretically be adsorbed. These models can be expressed by Eqs. (2) [41] and (3) [42]in the case of Langmuir and Freundlich adsorption, respectively:

$$\frac{C_e}{q_e} = \frac{C_e}{q_m} + \frac{1}{bq_m} \tag{2}$$

$$\log q_e = \log K_f + \frac{1}{n}\log C_e \tag{3}$$

where q_e is the equilibrium adsorption capacity of phosphate on the adsorbent (mg/g), C_e is the phosphate concentration in solution at equilibrium (mg/L), q_m represents the maximum amount of adsorbed phosphate as determined by the Langmuir isotherm model (mg/g), b is the adsorption constant of the Langmuir isotherm model, K_f (mg/g) is the Freundlich constant, and m (dimen-

Table 3. Constants and determination coefficients of the Langmuir and Freundlich isotherm models for phosphate adsorption

Type	Temp (K)	Langmuir isotherm			Freundlich Isotherm		
		q_m	b	R^2	K_f	n	R^2
γ-Al_2O_3	298	27.3	−3,458	1	26.7	41.3	0.640
Fh/γ-Al_2O_3 hybrid adsorbent	298	33.2	40.5	0.979	32.6	9.2	1

sionless) is the Freundlich exponent.

The Freundlich isotherm model is well known for describing both multilayer adsorption and adsorption on a heterogeneous surface, whereas the Langmuir isotherm model is valid for monolayer adsorption on a homogeneous active surface.

Both Langmuir and Freundlich adsorption can be evaluated by plotting the adsorption isotherm. The results of these calculations using the Langmuir adsorption model showed that the maximum amount that could be adsorbed was higher than that obtained with the Freundlich adsorption model. In the case of γ-Al_2O_3, the maximum adsorption amount by the Langmuir adsorption model was 27.3 mg/g, whereas the value obtained with the Freundlich adsorption model appeared to be 26.7 mg/g. In the case of the Fh/γ-Al_2O_3 hybrid adsorbent, the maximum adsorption amount obtained with the Langmuir and Freundlich adsorption models was 33.2 mg/g and 32.6 mg/g, respectively. Here, the correlation factor of the Freundlich isotherm plot had a lower value than the Langmuir isotherm. Therefore, we could confirm that the adsorption mechanism of the two adsorbents is governed by Langmuir adsorption.

To date, phosphate adsorption experiments were conducted using the batch adsorption performance test, the results of which are provided in Table 3. However, the batch adsorption experiment is difficult to apply in practice, whereas the column experiment is simple and easy to carry out.

Fig. 14 shows the breakthrough curve for the adsorption of phosphate ions on the Fh/γ-Al_2O_3 hybrid adsorbent in the column test. This curve was plotted using the C_e/C_o ratio as a function of time (where C_e and C_o represent the concentrations of the effluent and influent, respectively).

Process variables such as the adsorption equilibrium, mass transport, and the hydraulic conditions in the column determine the breakthrough curve. Commonly, a favorable adsorption breakthrough curve appears in the form of a step function. In the case of this column experiment, the breakthrough curve of favorable adsorption also follows the shape of a step function, as shown in Fig. 14.

ICP-OES was used to analyze the phosphate concentration at different time intervals after the phosphate solution passed through the column. The amount of adsorbent added to the column was 0.5 g with a particle size range of 180-300 μm. The phosphate solution, which was obtained by preparing a solution of phosphoric acid, passed through the bed volume at a flow rate of 10.25 BV/min (3.09 mL/min). As a result of its excellent adsorption performance, the Fh/γ-Al_2O_3 hybrid adsorbent mostly adsorbed the initial influent phosphate concentration of 4.75 mg/L, and, as it approached a state of saturation after 72 h, the effluent phosphate concentration became 4.33 mg/L, as shown in Fig. 14.

Fig. 15 shows the result of the phosphate adsorption efficiency and the maximum adsorption amount obtained by measuring the adsorbed amount as a function of time.

The column adsorption apparatus was designed to rely on gravity for flow. The result indicated that the initial phosphate concentration of 4.75 mg/L was adsorbed during a contact time of 5.85 s using 0.5 g of adsorbent with a size range of 180-300 μm.

Fig. 15 shows the result of measuring the adsorption efficiency of phosphate on the Fh/γ-Al_2O_3 hybrid adsorbent by using the column adsorption apparatus.

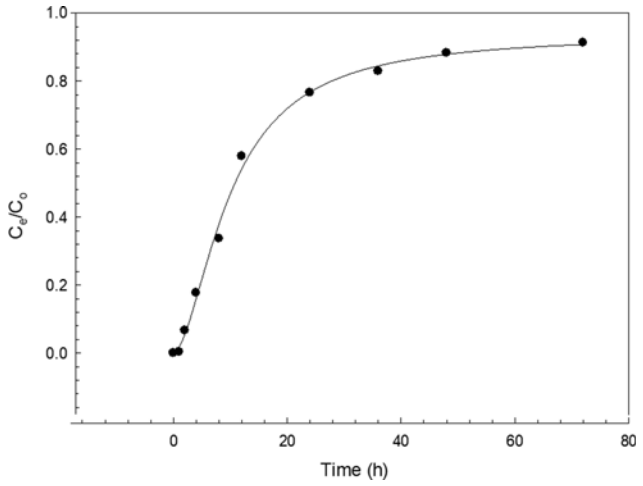

Fig. 14. Breakthrough curve of the Fh/γ-Al_2O_3 hybrid adsorbent for phosphate adsorption in the column test.

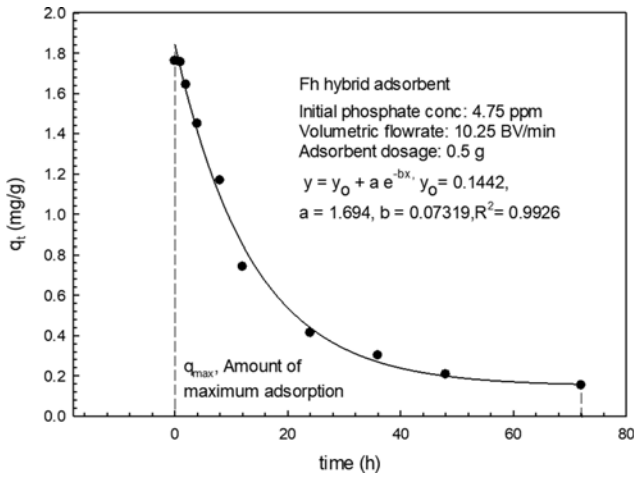

Fig. 15. Adsorption efficiency of the Fh/γ-Al_2O_3 hybrid adsorbent by column experiment.

Table 4. Constants and determination coefficient of the isotherm obtained by using the column adsorption apparatus for phosphate adsorption

Adsorbent	Temp (K)	Column adsorption test				
		Initial phosphate conc. (mg/L)	Adsorption time (h)	Volumetric flow rate	q_{max} (mg/g)	R^2
Fh/γ-Al_2O_3 hybrid adsorbent	298	4.75	72	10.25 BV/min (3.09 mL/min)	33.6	0.9926

Table 5. Efficiency of desorption of phosphate ions from the Fh/γ-Al_2O_3 hybrid adsorbent

Sample	pH_{des}	Maximum desorption conc. (mg/L)	Desorbed conc. (mg/L)	Desorption efficiency (%)
Fh/γ-Al_2O_3 hybrid adsorbent	12.5	36.96	26.65	72
	13.0	36.96	35.09	95

Table 4 summarizes the results of the experiments using the column.

The results in Fig. 15 were used to obtain the parameter for the f(t) equation by regressing the experimental f(t) data, which were well fitted by the basic equation $f(t)=\int_{t1}^{t2} y_o + ae^{-bt}dt$, which enabled the parameters y_o=0.1494, a=1.694, b=0.07368, and R^2=0.9926 to be established by regression. The equation is an exponential function with two parameters. On the other hand, $f(t)=\int_{t1}^{t2} y_o + ae^{-bt}dt$ could easily be solved by using an integral formula. The integral result for the period 0 to 72 h indicated that the maximum amount that was adsorbed appeared to be 33.6 mg/g in the case of the column adsorption experiment. This value was in good correspondence with the 33.2 mg/g obtained by the Langmuir adsorption isotherm model on the batch-type adsorption experiment. Thus, the value obtained in the column adsorption experiment was similar to the result obtained by calculating the Langmuir adsorption on the basis of the batch experiment.

The difference between the batch adsorption and column experiments is that the former is theoretical, whereas the latter is practical. Accordingly, the adsorption information gleaned from the column experiment must be useful in practice.

3. Desorption Studies

In the case of the Fh/γ-Al_2O_3 hybrid adsorbent based on EpHL [38,39], as shown in Fig. 10, phosphate adsorption occurs because of the surface charge of Fe-OH_2^+ as a result of the protonation of the adsorbent at pH<4.7 and desorption by the surface charge of Fe-O^- due to deprotonation of the adsorbent at pH>10. On the other hand, the range of 4.7<pH<10 coincides with that of the PZC of the adsorbent. These results suggest that adsorption is determined by factors such as dissolution, gathering, and dissociation of the phosphate, or the shape and polarity, and concentration of phosphate molecules, but factors such as electrostatic attractive and repulsive forces do not contribute to adsorption.

Accordingly, desorption of negatively charged phosphate ions from the surface of the Fh/γ-Al_2O_3 hybrid adsorbent quickly occurs above the inflection point of pH 11, as shown in Fig. 13. Based on this EpHL result, the pH conditions for desorption were determined by selecting the two pH values of pH 12.5 and pH 13.0 for the desorption experiment. The experimental results in Table 5 show that the desorption efficiency is 72% at pH 12.5 and 95% at pH 13.0. Accordingly, the optimal conditions for desorption could easily be found from the EpHL curve.

CONCLUSIONS

The granular Fh/γ-Al_2O_3 hybrid adsorbent was successfully synthesized from ferric sulfate wastewater through the precipitation and crystallization of 2-line Fh using γ-Al_2O_3 powder as a seed to induce mesopores and to enlarge the particle size of the adsorbent such that it is suitable for water treatment.

The synthesized Fh/γ-Al_2O_3 hybrid adsorbent had a Langmuir surface area of 334 m^2/g, BET surface area of 260 m^2/g, and mesopore size of 4.03 nm. The PZC value of the synthesized hybrid adsorbent was 4.82.

The batch adsorption experiment revealed the maximum amount of synthesized Fh/γ-Al_2O_3 hybrid adsorbent to be 33.2 mg/g, as determined by using the Langmuir isotherm model for a concentration range from 0 to 10 mg/L. In the case of the column test, the maximum adsorption capacity was 33.6 mg/g after adsorption for 72 h at an initial phosphate concentration of 4.75 mg/L. The maximum adsorption capacity of the column test almost coincided with the maximum adsorption capacity determined by the batch test. Accordingly, these batch and column experiments confirmed that the adsorption isotherm model was governed by Langmuir adsorption.

The synthesized Fh/γ-Al_2O_3 hybrid adsorbent differed from the pure Fh adsorbent in that the strong electrostatic adsorption was additionally induced on the Langmuir adsorption at the initial phosphate concentration of 4.75 ppm in the column test.

This study showed that the superior adsorption of the Fh/γ-Al_2O_3 hybrid adsorbent is attributable to the addition of γ-Al_2O_3, of which the PZC value of 9.50 is higher than that of the Fh adsorbent of 4.30. The phosphate recovery efficiency was also high at 95% at pH 13, based on the PZC result.

In conclusion, we confirmed that the PZC value of the adsorbent and the pH of the solution are key factors for designing a

highly efficient adsorbent and demonstrated that the synthesized Fh/γ-Al_2O_3 hybrid adsorbent could be a useful alternative for water remediation.

ACKNOWLEDGEMENTS

This research was supported by the Basic Science Research Program through the National Research Foundation of Korea (NRF) funded by the Ministry of Education (Project No.: 2019R1I1A1 A01041329). Solid-state NMR experiments were carried out on the Bruker AVANCES II+ 400 MHz NMR system and FE-SEM (in KBSI Seoul Western Center) and the XRD measurements were conducted on the X-ray diffractometer (in KBSI Seoul Center).

NOMENCLATURE AND UNITS

b : adsorption constant of the Langmuir isotherm model [mg/g]
C_o : initial phosphate concentration [mg/L]
C_e : equilibrium phosphate concentration [mg/L]
K_f : Freundlich constant [mg/g]
m : mass of the adsorbent [g]
n : Freundlich exponent, dimensionless
pH_{des} : pH of desorption
q_e : equilibrium capacity of phosphate [mg/g]
q_m : maximum amount of adsorbed phosphate by Langmuir isotherm model [mg/g]
q_{max} : maximum amount of adsorbed phosphate in column test [mg/g]
R^2 : correlation factor
V : volume of phosphate solution [mL]

Greek Letter

γ : gamma

REFERENCES

1. D. Carta, M. F. Casula, A. Corrias, A. Falqui, G. Navarra and G. Pinna, *Mater. Chem. Phys.*, **113**, 349 (2009).
2. X. Wang, W. Li, R. Harrington, F. Liu, J. B. Parise, X. Feng and D. L. Sparks, *Environ. Sci. Technol.*, **47**, 10322 (2013).
3. F. M. Michel, L. Ehm, S. M. Antao, P. L. Lee, P. J. Chupas, G. Liu, D. R. Strongin, M. A. A. Schoonen, B. L. Phillips and J. B. Parise, *Science*, **316**, 1726 (2007).
4. J. C. Mendez and T. Hiemstra, *Chem. Geol.*, **532**, 119304 (2020).
5. T. S. Peretyazhko, S. J. Ralston, B. Sutter and D. W. Ming, *J. Geophys. Res.-Planets*, **125**, 1 (2020).
6. A. Namayandeh and N. Kabengi, *J. Colloid Interface Sci.*, **540**, 20 (2019).
7. K. Rout, M. Mohapatra and S. Anand, *Dalton Trans.*, **41**, 3302 (2012).
8. S. Das, M. J. Hendry and J. Essilfie-Doughan, *Environ. Sci. Technol.*, **45**, 5557 (2011).
9. Z. Liu, Y. Lu and X. Duan, *Int. J. Environ. Anal. Chem.*, https://doi.org/10.1080/03067319.2020.1779246 (2020).
10. E. H. Winstanley, K. Morris, L. G. Abrahamsen-Mills, R. Blackham and S. Shaw, *J. Hazard. Mater.*, **366**, 98 (2019).
11. Y. Liang, L. Tian, Y. Lu, L. Peng, P. Wang, J. Lin, T. Cheng, Z. Dangab and Z. Shi, *Environ. Sci.: Processes Impacts*, **20**, 934 (2018).
12. J. Zhu, M. Pigna, V. Cozzolino, A. G. Caporale and A. Violante, *Geoderma*, **159**, 409 (2010).
13. S. Zhou, T. Sato and T. Otake, *Minerals*, **8**, 101 (2018).
14. A. J. Hobson, D. I. Stewart, A. W. Bray, R. J. G. Mortimer, W. M. Mayes, A. I. Riley, M. Rogerson and I. T. Burke, *Sci. Total Environ.*, **643**, 1191 (2018).
15. S. Das, J. Essilfie-Dughan and M. J. Hendry, *Appl. Geochem.*, **73**, 70 (2018).
16. S. Kikuchi, T. Kashiwabara, T. Shibuya and Y. Takehashi, *Geochim. Cosmochim. Acta*, **251**, 1 (2019).
17. J. A. Arcibar-Orozco, R. Wallace, J. K. Mitchell and T. J. Bandosz, *Langmuir*, **31**, 2730 (2015).
18. T. Mathew, K. Suzuki, Y. Ikuta, Y. Nagai, N. Takahashi and H. Shinjoh, *Angew. Chem. Int. Ed.*, **50**, 7381 (2011).
19. H. Osawa, J. Lohwacharin and S. Takizawa, *Sep. Purif. Technol.*, **176**, 184 (2017).
20. L. A. Chiavacci, K. Dahmouche, N. J. O. Silva, L. D. Carlos, V. S. Amaral, V. Bermudez, S. H. Pulcinelli, C. V. Santilli, V. Briois and A. F. Craievich, *J. Non-Crystalline Solids*, **345**, 585 (2004).
21. A. R. Wallace, C. Su and W. Sun, *Environ. Eng. Sci.*, **36**, 634 (2019).
22. G. Li, D. Chen, W. Zhao and X. Zhang, *J. Environ. Chem. Eng.*, **3**, 515 (2015).
23. S. Yang, Y. Zhao, R. Chen, C. Feng, Z. Zhang, Z. Lei and Y. Yang, *J. Colloid Interface Sci.*, **396**, 197 (2013).
24. L. Lai, Q. Xie, L. Chi, W. Gu and D. Wu, *J. Colloid Interface Sci.*, **465**, 76 (2016).
25. D. Mitrogiannis, M. Psychoyou, I. Baziotis, V. J. Inglezakis, N. Koukouzas, N. Tsoukalas, D. Palles, E. Kamitsos, G. Oikonomou and G. Markou, *Chem. Eng. J.*, **320**, 510 (2017).
26. F. Li, W. Wu, R. Li and X. Fu, *Appl. Clay Sci.*, **132**, 343 (2016).
27. Z. Ren, L. Shao and G. Zhang, *Water Air Soil Pollut.*, **223**, 4221 (2012).
28. X. Huang, G. D. Foster, R. V. Honeychuck and J. A. Schreifels, *Langmuir*, **25**, 4450 (2009).
29. E. Chmielewská, R. Hodossyová and M. Bujdoš, *Pol. J. Environ. Stud.*, **5**, 1307 (2013).
30. B. J. Kang, *J. Adv. Eng. Technol.*, **4**, 475 (2011).
31. C. A. Fyte, G. C. Gobbl, J. S. Hartmen, J. Kllnowski and J. M. Thomas, *J. Phys. Chem.*, **86**, 1247 (1982).
32. S. Komarneni, R. Roy and D. M. Roy, *Cem. Concr. Res.*, **15**, 723 (1985).
33. T. R. Lopes, G. R. Goncalves, E. de Barcellos Jr., M. A. Schettino Jr., A. G. Cunha, F. G. Emmerich and J. C. C. Freitas, *Carbon*, **93**, 751 (2015).
34. D. Muller, W. Gessner, H.-J. Behrens and G. Scheler, *Chem. Phys. Lett.*, **79**, 59 (1981).
35. L. F. Nazar and L. C. Klein, *Commun. Am. Ceram. Soc.*, **71**, C-85 (1988).
36. L. Samain, A. Jaworski, M. Eden, D. M. Ladd and D. K. Seo, *J. Solid State Chem.*, **217**, 1 (2014).
37. P. S. Kumar, T. Prot, L. Korving, K. J. Keesman, I. Dugulan, M. C. M. van Loosdrecht and G. J. Witkamp, *Chem. Eng. J.*, **326**, 231 (2017).
38. J. R. Regalbuto, *Catalyst preparation science and engineering*, CRC Press, New York (2007).

39. R. Richards, *Surface and nanomolecular catalysis*, CRC Press, New York (2006).
40. A. Ghosh, S. Paul, S. Bhattacharys, P. Sasikumar, K. Biswas and U. C. Ghosh, *Environ. Sci. Pollut. Res.*, **26**, 4618 (2019).
41. I. Langmuir, *J. Am. Chem. Soc.*, **40**, 1361 (1918).
42. H. M. F. Freundlich, *Z. Phys. Chem-Frankf.*, **57A**, 385 (1906).